PCCP

PAPER

View Article Online
View Journal

Cite this: DOI: 10.1039/c5cp01017a

Gas molecule scattering & ion mobility measurements for organic macro-ions in He *versus* N_2 environments

Carlos Larriba-Andaluz,*[a] Juan Fernández-García,[b] Michael A. Ewing,[c] Christopher J. Hogan Jr.[a] and David E. Clemmer[c]

A pending issue in linking ion mobility measurements to ion structures is that the collisional cross section (CCS, the measured structural parameter in ion mobility spectrometry) of an ion is strongly dependent upon the manner in which gas molecules effectively impinge on and are reemitted from ion surfaces (when modeling ions as fixed structures). To directly examine the gas molecule impingement and reemission processes and their influence, we measured the CCSs of positively charged ions of room temperature ionic liquids 1-ethyl-3-methylimidazolium dicyanamide (EMIM-$N(CN)_2$) and 1-ethyl-3-methylimidazolium tetrafluoroborate (EMIM-BF_4) in N_2 using a differential mobility analyzer-mass spectrometer (DMA-MS) and in He using a drift tube mobility spectrometer-mass spectrometer (DT-MS). Cluster ions, generated *via* electrosprays, took the form $(AB)_N(A)_z$, spanning up to z = 20 and with masses greater than 100 kDa. As confirmed by molecular dynamics simulations, at the measurement temperature (~300 K), such cluster ions took on globular conformations in the gas phase. Based upon their attained charge levels, in neither He nor N_2 did the ion-induced dipole potential significantly influence gas molecule–ion collisions. Therefore, differences in the CCSs measured for ions in the two different gases could be primarily attributed to differences in gas molecule behavior upon collision with ions. Overwhelmingly, by comparison of predicted CCSs with selected input impingement–reemission laws to measurements, we find that in N_2, gas molecules collide with ions diffusely – they are reemitted at random angles relative to the gas molecule incoming angle – and inelastically. Meanwhile, in He, gas molecules collide specularly and elastically and are emitted from ion surfaces at determined angles. The results can be rationalized on the basis of the momentum transferred per collision; in the case of He, individual gas molecule collisions minimally perturb the atoms within a cluster ion (internal motion), while in the case of N_2, individual gas molecules have sufficiently large momentum to alter the internal motion in organic ions.

Received 17th February 2015,
Accepted 29th April 2015

DOI: 10.1039/c5cp01017a

www.rsc.org/pccp

Introduction

Ion mobility spectrometry (IMS) is widely used for the characterization of sub-nanometer to micrometer sized charged entities (ions), including biomolecules,[1–9] explosives,[10] polymers,[11–15] ambient aerosol particles,[16,17] and metal[18] and metal oxide[19] nanoparticles. Despite the increasing use of IMS in laboratory, clinical,[20,21] and environmental[16] settings, there remain difficulties in understanding the manner in which ions interact with gas molecules as they drift through the separation regions of IMS devices. A linearized solution for the mobility of ions (Z_p), referred to as the Mason–Schamp equation[22] and which is approximately valid for ions moving at a low speed relative to the bath gas mean thermal speed, states that under constant gas conditions of temperature and pressure, and large mean free path relative to the ion size, the ion mobility is proportional to the ratio of the ion's charge state (z) to its collisional cross section (CCS), Ω:

$$Z_p = \sqrt{\frac{9\pi}{128 m_{red} n_{gas}{}^2 k T}}\frac{ze}{\Omega}, \quad (1)$$

where k is the Boltzmann constant, T is the gas temperature, n_{gas} is the gas molecule number concentration, m_{red} is the reduced mass of the ion–gas molecule system, and e is the unit elementary charge. In contrast to the other easily defined parameters on the right-hand side of eqn (1), the CCS (also referred to as the first collision integral) is a very intricate parameter,

[a] University of Minnesota, Mechanical Engineering Department, 111 Church st. RM 2101A, Minneapolis, MN, 55455, USA. E-mail: clarriba@umn.edu
[b] Yale University, Mechanical Engineering Department, PO Box 208286, New Haven, CT 06520-8286, USA
[c] Indiana University, Department of Chemistry, Bloomington, IN 55455, USA

quantifying the extent to which the momentum is transferred from gas molecules to ions upon close approach;[23–32] hence it is dependent on ion–gas molecule interactions. There is considerable interest in calculating the CCS for model ion structures in bath gases in which measurements are made, which enables the application of IMS not only for ion separation, but also for approximate identification of the ion structure in the gas phase.[13,33–40] However, ambiguities in modeling gas molecule–ion dynamics can hinder the possibility of linking the ion structure to the CCS (and measured mobilities). Although in prior studies the CCS has been equated with orientally averaged physical cross section of an ion in the gas phase,[41,42] the collisional cross section is also dependent on parasitic effects that increase its value beyond an ion's projected area and which are in many instances difficult to describe *a priori*. Of particular difficulty is modeling the multiple gas molecule scattering influence[24] (*i.e.* the enhancement of the CCS caused by multiple collisions that occur from the same gas molecule) coupled with:

(1) The exchange of energy between vibrational and translational degrees of freedom of the atoms inside the ion and those of the gas molecule.[27–30]

(2) Both short and long range potential energy changes (including Lennard-Jones and ion-induced dipole potentials).[23,27]

(3) The change in ''gas molecule–gas molecule'' collision dynamics brought about by the presence of a sufficiently large ion.[43]

(4) Changes to the ion structure which may be brought about by gas molecule close approach and impingement.

For complex, corrugated ion structural models (*i.e.* all-atom structural models as well as coarse-grained models of large ions with polyatomic base units[2,44]), Monte Carlo algorithms are the most tractable approach for CCS calculations, in which gas molecules are seeded with an initial velocity near an ion, and each gas molecule's trajectory is monitored to infer the rate of momentum transfer (which leads to the drag force on the ion as well as its CCS). A number of such algorithms have been developed for this purpose.[7,23–28,31,32,42,44,45] In all developed CCS calculation algorithms to date, several simplifications have been made, the most important of which is that the atoms/base units within the ion remain fixed. While this choice significantly speeds up calculations, particularly when hard-sphere interactions are used, it invariably leads to the need to choose a reemission law defining the manner (angle and speed) in which gas molecules are released from the ion surface upon collision. Regrettably, to date, there has been no widely accepted reemission law which can be invoked universally for all ions and all bath gases.[29,30]

At present, there are two reemission laws employed in CCS calculations, the elastic specular hard sphere scattering model (EHSS)[24] and the inelastic diffuse hard sphere scattering model (DHSS).[27,28] In the former, momentum transferring collisions are assumed to be between a ''frozen'' ion and moving, spherical gas molecules. EHSS model collisions are thus regarded as completely specular (with deterministic reemission angles) as well as elastic. In this instance, the CCS enhancement over the projected area of the ion only arises from reiterative collisions of a spherical gas molecule with different atoms of the structure (multiple collision events). This type of scattering therefore increases the CCS by an amount which depends only on the roughness of the structure in comparison to the size of the gas molecule. The assumptions of the EHSS model (specular, elastic collisions) are further implicit in CCS calculations where Lennard-Jones potential interactions are modeled between all atoms within an ion and the gas molecule (*i.e.* so-called trajectory methods). Conversely, in DHSS models, though the atoms in the ion structure still remain fixed, a semi-empirical law after gas molecule impingement is brought forth to mimic how the collisions would behave if the atoms involved were vibrating and rotating, *i.e.* non-modeled degrees of freedom in both the ion and the gas molecule are considered in energy conservation. While a number of DHSS models can be developed,[46] in the most common one, chosen to match a number of experimental results,[13,47–52] gas molecule velocities post-collision are sampled from a Maxwell–Boltzmann distribution at the ion temperature (mimicking a maximal exchange between ion internal energy and gas molecule translational energy) and the angle of reemission is sampled randomly. The DHSS model therefore leads to an increase in CCS over the projected area due to not only multiple gas molecule scattering collisions, but also the diffuse and inelastic nature of each individual collision.

When using all-atom models of ion structures, the EHSS model (and related trajectory methods with implicitly assumed specular-elastic collisions) has been and continues to be the most commonly used approach for CCS calculations. However, from a theoretical point of view, it is clear that the EHSS model is not rigorously valid for any ion in any bath gas, as to maintain thermal equilibrium between the ion and the gas molecule there must be some degree of thermal energy exchange upon collision. With that said, in terms of CCS calculations the question becomes how important are the effects of energy exchange on CCSs and to what extent must they be considered in calculations. A number of studies find reasonable agreement between EHSS model predictions and CCSs inferred from measurements in He of small ($<$1000 Da) ions,[6,23–25,32,53] suggesting that, in this instance, internal energy exchange on a per collision basis minimally influences gas molecule momentum transfer to an ion. Conversely, in N_2 and air and for larger organic and inorganic ions ($>$1000 Da), DHSS model predictions find better agreement with experimental measurements.[13,28,49,50,54–56] However, recent work examining iodide salt cluster ions in air highlights that neither the EHSS model nor the DHSS model can be universally applied in CCS calculations.[29] Furthermore, with incorporation of Lennard-Jones potential parameters (with *ad hoc* parameters to match experimental measurements), prior work[7] has adapted trajectory method calculations developed for He (with assumed specular collisions) to find a reasonable agreement with measurements of small ions in N_2.

There is hence remaining ambiguity in how to perform CCS calculations to compare model structures to measurements, particularly in diatomic gases.[57] Aside from the arduous task of coupling molecular dynamics (MD) to CCS calculations (wherein all atomic motion in gas molecules and ions is incorporated), a

practical way to examine these scattering effects is by comparing experimental results with numerical calculations of simple ions whose structures can be inferred with little uncertainty from MD calculations. Along these lines the purpose of this work is to attempt to resolve ambiguities in how to practically perform CCS calculations for large organic ions in both helium and nitrogen, with an emphasis on examining how different reemission rules influence calculations. We specifically focus on large organic ions because of the considerable interest in using IMS for biomolecular analysis,[1–3,58,59] and the previously attained results for inorganic ions[29] which do not yet yield a universal reemission law to employ. As model ions, we examine multiply charged cluster ions generated from two different room temperature ionic liquids (RTILs), 1-ethyl-3-methylimidazolium dicyanamide (EMIM-N(CN)$_2$) and 1-ethyl-3-methylimidazolium tetrafluoroborate (EMIM-BF$_4$), and measure their mobilities in helium and diatomic nitrogen, with subsequent mass analysis (IMS-MS experiments). Important advantages of RTILs in this effort are that (1) they are of low volatility, minimizing the often observed dissociation post-IMS analysis and prior to MS analysis,[60] (2) when electrosprayed in high enough concentration, RTILs arrange themselves as globular aggregates with sizes ranging between 1 and ~9 nm, which consist of hundreds to several thousands of atoms,[50,61–63] and with charge states varying from 1 upwards of 20+ charges, (3) they, as liquids, cannot adopt highly stretched/linear structures (as compared to highly charged proteins or polymers[13,14]) and, in the size range of interest, they have density close to known bulk values,[50,62,63] (4) large data sets for the mobilities of ions of known chemical composition are attained using only one experiment (the relation between characteristic ion mobilities is thus not affected by variations of temperature or pressure of the instrument between experiments), and (5) the contribution of the ion induced dipole potential to CCS calculations (which can be large for small ions in nitrogen bath gas) is minimized, as the charge on RTIL cluster ions has a ceiling defined by either the Rayleigh limit or ion evaporation kinetics.[61] Collectively, this suggests that the difference in CCSs measured in different gases will be primarily due to the extent to which collisions are elastic or inelastic for these ions. The sections that follow describe in detail the generation of RTIL cluster ions and their measurement *via* IMS-MS, the development of structural models for the analyzed ions, and the comparison of measured collisional cross sections to theoretical predictions with different assumed gas molecule impingement–reemission rules invoked.

Experimental setup and methods

Two distinct ion mobility spectrometers were used for measurements: (1) a parallel-plate differential mobility analyzer (DMA; model P4 SEADM; resolution near 60)[64] coupled to a QSTAR XL time-of-flight (TOF) mass spectrometer (DMA-MS) and (2) a custom-built 3 meter drift tube ion mobility spectrometer coupled to a mass spectrometer (DT-MS, resolution in excess of 100). Though different setups were employed, we remark that

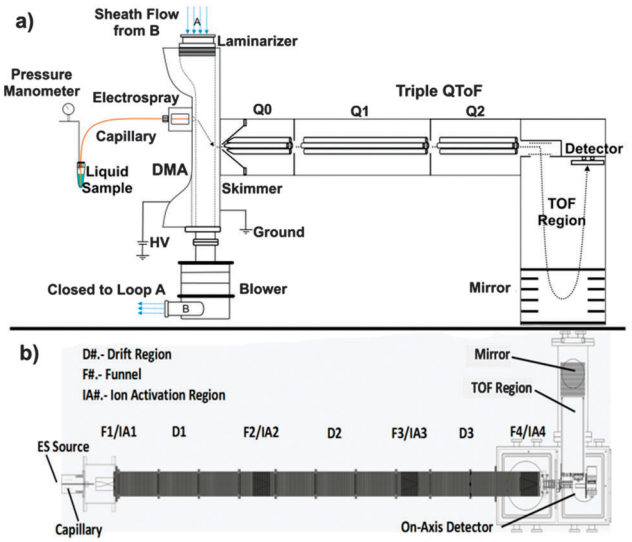

Fig. 1 Depictions of the two IMS-MS setups used, relying either on (a) a differential mobility analyzer, DMA, or (b) a 3 m drift tube.

the use of these two different instruments does not alter in any way the results or conclusions shown herein for the following reasons:

(1) Both instruments used follow the same principle. That is, a constant electric field pulls the charged particles or ions through a gas medium separating such ions through their ability to traverse this medium.

(2) The results presented in this work for comparison between He and N_2 are not presented as raw collisional cross section (CCS) comparisons between gases but as ratios of CCSs to their average projected areas, as well as how the CCS to projected area ratio scales with the ion size (diameter). A comparison made in this manner largely mitigates the influence of different instrument setups, and further diminishes the influence of different calibration approaches.

Both experimental setups are depicted in Fig. 1, and a limited overview of each of the systems is provided here, including the specific details on the RTIL cluster ion generation techniques employed. Further explanation of the operation of the ion mobility spectrometers is provided in prior work for the DMA-MS[61,64] and the DT-MS[65] respectively.

Differential mobility analyzer-mass spectrometer (DMA-MS)

DMAs are mobility filters which transmit continuous beams of ions with mobilities falling within a certain narrow band, the width of which is defined by the DMA resolution.[66] Analogous to the operation of a quadrupole mass filter, mobility spectra can be recorded by varying the DMA operational settings (applied voltage and sheath gas flow rate). As DMAs typically operate near atmospheric pressure, they can be installed on the front end of nearly any mass spectrometer which utilizes an atmospheric pressure ionization (API) source, provided the DMA outlet is properly integrated with the MS inlet to facilitate high ion transmission. Accordingly, a flat parallel plate DMA has been installed in front of a MD Sciex QSTAR triple quadrupole TOF

mass spectrometer (m/z range $\sim$40 000; resolving power $\sim$10 000) and used for measurements here. Dry nitrogen gas was used as the sheath flow (with the recirculating sheath flow rate maintained using a Domel vacuum blower) at a pressure of $\sim$1 atmosphere and a temperature of 35 °C, which was measured at the entrance of the DMA with a thermocouple. At the DMA inlet (on the front plate electrode), for each experiment, a solution of either 10–20 mM EMIM-$N(CN)_2$ or EMIM-BF_4 in methanol or acetonitrile was electrosprayed from a Polymicro silica capillary (inner diameter: 40 μm, outer diameter: 360 μm). Each solution was introduced into the capillary by placing it in a 1.5 ml polypropylene vial; the vial was pressurized above atmospheric pressure so as to permit a flow of liquid to be pushed through a capillary, and through a platinum wire in the vial the liquid was raised to a potential of $\sim$2 kV above the front plate of the DMA using an EMCO high voltage power supply. At its outlet, the outer diameter of the silica capillary was carefully tapered down to $\sim$80 micrometers to facilitate better anchoring of the meniscus of the electrospray cone, which lowers the onset voltage needed for electrospray. The capillary tip was aligned with the inlet of the DMA at a distance of $\sim$2 mm away from the slit, and a counterflow of 0.1–0.2 l min^{-1} was used to prevent any non-charged species from entering the DMA.

For a mean sheath flow velocity, U, as well as the applied potential V_{DMA}, the mobility of an ion transmitted from the DMA inlet to the outlet is given by the equation:

$$Z_p = \frac{U\delta^2}{LV_{DMA}} \quad (2)$$

where δ is the distance between DMA electrodes and L is the axial distance (along the plates) from the inlet to the outlet. However, since the velocity was not measured directly, a calibrant, the tetraheptylammonium (THA) bromide dimer, $(THABr)THA^+$, with an atmospheric pressure mobility of 0.984 $cm^2\ V^{-1}\ s^{-1}$ at 31 °C was used to infer a reference value for V_{DMA}.[62] For the EMIM-BF_4 spectra, the dimer appeared at 1600 V, while for EMIM-$N(CN)_2$ the tetralkylammonium monomer was used to calibrate the 62^{+4} cluster (m/z = 2857.9 Thomsons) with a reduced mobility of 0.5966 $cm^2\ V^{-1}\ s^{-1}$ at 20 C occurring at 2419 V.

Upon exiting the DMA, the ions enter the mass spectrometer through an inlet wherein the pressure is of reduced orders of magnitude, from one atmosphere to $\sim$1 Torr. As noted in prior studies, in this region cluster ions may partially dissociate, losing one or several neutral cation–anion (AB) pairs,[60] or a positively charged (for positive ions) cluster composed of two cations and one anion $(AB)A^+$.[61] This effect is enhanced when the declustering potentials are applied at the inlet. For this reason, we chose to keep the declustering potentials set to 0 volts. Tandem mass-mobility spectra were gathered by measuring a time-of-flight mass spectrum for each selected value of V_{DMA} (in steps of 10 V), with a constant DMA sheath flow rate. For each electrosprayed sample, a two dimensional m/z *vs.* Z_p spectrum was produced by assigning a color coded dimension to the logarithm of the ion signal intensity. Data were then post-processed using MATLAB.

Drift tube ion mobility spectrometry-mass spectrometry (DT-MS)

The drift tube employed consisted of a 3 m long low pressure ($\sim$3 Torr) He tube cell (Bloomington, Indiana).[67–69] In it, a constant decrease in voltage through equally spaced resistors led to a constant electric field, E, which directed the ions along the tube's length L_d, while separating them in drift time t_D according to their inverse mobility:

$$Z_p = \frac{L_D}{t_D E} \quad (3)$$

The drift tube was interfaced with a custom-made TOF mass spectrometer, which was synchronized with the bursts of ions that were introduced into it from the drift tube by a pulsating gate. For every pulse of ions introduced into the drift tube, which required several miliseconds to traverse the tube, several hundred of pulses at drift-time-defined intervals were used to release ions into the mass spectrometer at the drift tube outlet. In this manner, tandem mass-mobility spectra were collected. To reach appreciably high signal-to-noise ratios, the spectra were integrated over multiple drift tube measurements. As with DMA calibration, the mobility of the examined ions was not inferred directly from instrument dimensions, but was instead inferred from the measurement of a calibrant ion, in this instance, a doubly charged bradykinin ion, which has a collisional cross section of 246 A^2 in helium.[70]

To introduce cluster ions into the drift tube, a methanol solution of 0.1–0.3% by volume EMIM-$(CN)_2$ or EMIM-BF_4 was electrosprayed from a polyamide coated silica capillary (OD: 360 μm; ID: 100 μm, reduced to approximately 40 μm at the tip). The solution was driven through the capillary using a syringe pump (KD Scientific) and a 500 μl syringe (Hamilton) at a rate of approximately 8 μl h^{-1}. A Bertan high voltage power supply floating 2.2 kV was used to form stable electrosprays. Just prior to the ion funnel trap in the drift tube IMS-MS, there was a drop of pressure from 1 atmosphere to 3 Torr, wherein similar to the high pressure drop region of the DMA-MS system, cluster ion dissociation reactions may have occurred. However, as in the DT-MS system, this region was upstream of the mobility measurement; such reactions would not have been detectable in mass-mobility spectra. Similar to mass-mobility spectra from DMA-MS measurements, DT-MS m/z *vs.* Z_p spectra were processed using MATLAB, and for plotting purposes a color code was assigned to the logarithm of the measured signal intensity.

Molecular dynamics simulations

Molecular dynamics simulations were used to generate EMIM-$N(CN)_2$ and EMIM-BF_4 cluster ion candidate structures, which in turn were used for CCS predictions and comparison to measurements (as described in the Results & discussion section). In all calculations, the MM2 force-field[71] was applied. The structures analyzed were composed of a specific number of neutral cation–anion pairs N, with the cation as $EMIM^+$ and the anion as $N(CN)_2^-$ or BF_4^-, depending on which RTIL was modeled. N = 16, 32, 64, 128, 256, 512 and 832 ($\sim$20 000 atoms) were modeled for EMIM-$N(CN)_2$, while N = 18, 36, 50, 78, 156

and 312 were modeled for EMIM-BF_4. The smallest N simulations were initiated by adding neutral ion pairs in random locations, and allowing all atom positions to evolve in time. Initial conditions for larger N structures were then constructed by doubling structures obtained for smaller systems. In all instances, independent of the initial configuration, globular configurations were obtained within several picoseconds of simulation time. After obtaining such structures, several cycles of simulated annealing were performed, in which the simulation temperature was increased, and then cooled, to ensure that a structure near the global energy minimum structure was obtained. Structures were then allowed to stabilize at 300 K, close to the measurement temperature. In selected instances, several excess cations ($EMIM^+$) were added to structures to examine if such excess charges led to deformation of structures. However, it was found that for experimentally attainable excess charge levels, excess cations did not alter the physical cross sections of structures obtained in simulations.

Depictions of cluster ion structures resulting from simulations are provided in Fig. 2 for both RTILs. Prior to incorporating structures into collisional cross section calculations, we remark that it is essential that the overall size of structures be correctly scaled by comparison to reference values; molecular dynamics simulations give rise to structures whose physical dimensions are strongly dependent on the input potentials (which govern the resulting interatomic distances). As the physical size of an ion is one of the largest contributors to its CCS, incorrectly sized structures must be rescaled for accurate CCS predictions. Fortunately, for the largest RTIL clusters examined, there is strong evidence that structures will have densities close to those of bulk RTILs,[49,50] and further near room temperature the densities of EMIM-BF_4 and EMIM-$N(CN)_2$ are known to be 1290 Kg m^{-3} and 1111 Kg m^{-3}, respectively.[72] To scale structures in accordance with these values we calculated the solvent accessible volume (with a 1.4 Å probe) for the largest simulated EMIM-$N(CN)_2$ and EMIM-BF_4, with N = 832 and N = 312, respectively. As the mass of these clusters is known exactly, volume calculation enabled direct determination of the density. In both cases, we observed that the density was underestimated, by 11.7% for EMIM-$N(CN)_2$ and ~10.7% for EMIM-BF_4, similar to findings of polyethylene glycol structures obtained from simulations using the same force field.[28] Based on this result, all obtained structures from molecular dynamics were rescaled, such that their volumes were reduced by 11.7% and 10.7% for EMIM-$N(CN)_2$ and EMIM-BF_4 cluster ions, respectively.

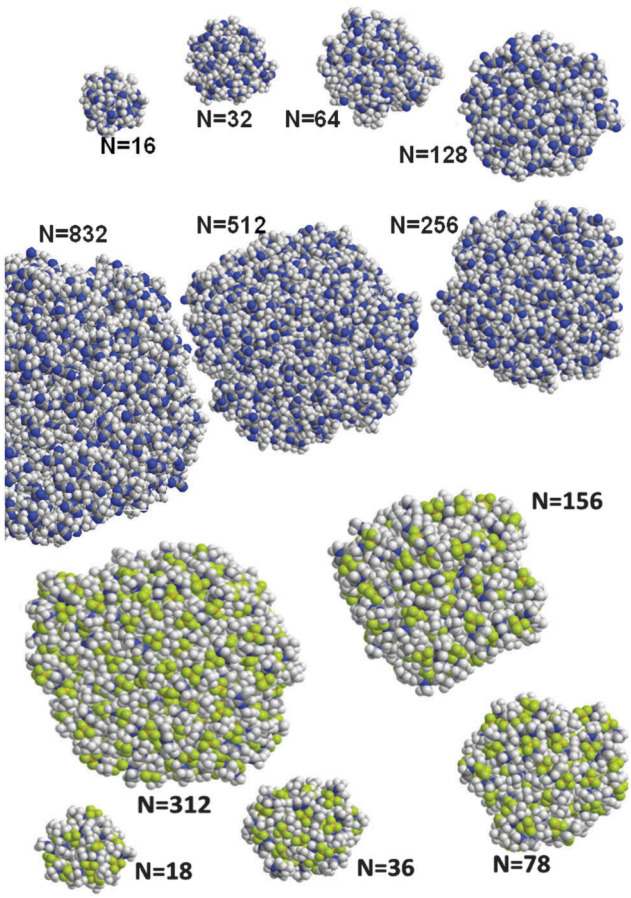

Fig. 2 Depictions of candidate cluster ion structures resulting from molecular dynamics simulations of EMIM-$N(CN)_2$ (top) and EMIM-BF_4 (bottom). N denotes the number of pairs used in each model. The resulting structures were globular regardless of the initial position of the neutral pairs utilized.

Results and discussion

Collisional cross section inference from measurements

Fig. 3 displays contour plots of the measured signal intensity (depicted by color, with blue for low intensity and red for high intensity) *versus* the raw measured parameter proportional to the inverse mobility (inverse mobility itself, $1/Z$, for DMA-MS and drift time for DT-MS) and m/z, for both EMIM-$N(CN)_2$ and EMIM-BF_4.

DMA-MS measurements in N_2 are shown on the right side of the figure, while DT-MS measurements in He are provided on the left side. Depictions of the cation (A) and anion (B) in both RTILs are provided in the figure as well. We first remark on several features evident in these spectra followed by the discussion of conversion of measurements to CCSs for mass identified structures, leading to a direct comparison of CCS predictions for simulated candidate structures, and finally the implications of the reported measurements.

All collected cluster ion spectra are similar to one another; as has been noted in prior work,[28,29,60–63] cluster ions produced *via* positive mode electrospray have the chemical formula $(AB)_NA^+_z$, and in mass-mobility contour plots (such as those in Fig. 3) each detected cluster ion leads to a line segment whose thickness (in the vertical direction) is determined by the mass spectrometer resolution and degree of mass averaging, while the width (in the horizontal direction) is governed by the resolution of the mobility spectrometer. As higher N cluster ions also have higher z, line segments for all ions of a specific z are grouped into identifiable bands in contour plots, with

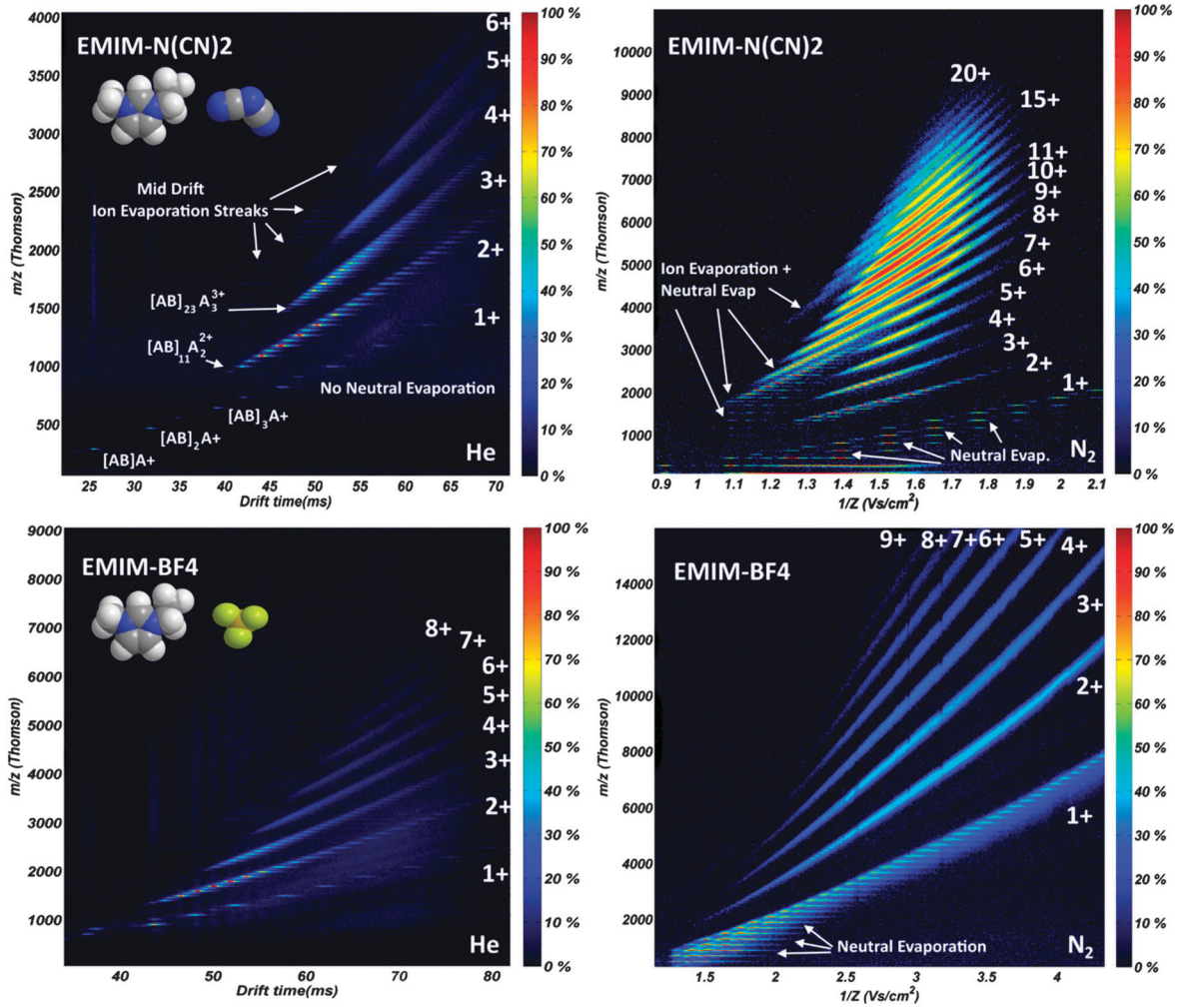

Fig. 3 Mass-mobility contour plots for EMIM-N(CN)$_2$ (top) and EMIM-BF$_4$ (bottom) cluster ions measured in two different gases: He (left, measured by DT-MS) and N_2 (right, measured by DMA-MS). Charge states (z) are labeled for identifiable bands. Selected species are labeled noting the number of neutral pairs and the excess cations: $[AB]_N A^{z+}{}_z$.

larger z bands appearing at progressively higher m/z ratios. The increase in m/z between neighboring line segments within the same band represents the mass of one cation–anion pair, hence line segments in higher z bands are closer to one another. Eventually, the attachment of impurities to ions prevents a clear identification of line segments; for example, although the resolution in m/z should be sufficient to distinguish $z > 5$ species in all circumstances, only for several specific cluster ions it is possible. Nonetheless, because of the known band structure for cluster ions of a specific z in mass-mobility contour plots, it is possible to identify cluster ions with z up to 6 in all circumstances, and upwards of 20 for EMIM-N(CN)$_2$ cluster ions in DMA-MS measurements.

Also in DMA-MS contour plots, there is evidence for several dissociation reactions occurring for some clusters ions as they transited between the differential mobility analyzer and the mass spectrometer. These reactions likely occur in the high pressure drop interface region, thus they are not detected in DT-MS analysis;[14] they would have occurred prior to both mobility and mass analyses. For charge state $z = 1$, several line segments appear spanning identical inverse mobility ranges, but differing in mass by successive AB units. Such line segments are the result of neutral pair evaporation/dissociation.[29,60] Therefore, the line segments appear at an inverse mobility corresponding to the inverse mobility of the parent ion only; they are not evidence of multiple conformers of singly charged cluster ions. Similar to neutral evaporation, several clusters undergo ion evaporation between the DMA and the MS, where the cluster $(AB)A^+$ typically dissociates once or several times. Ion evaporation events lead to progeny ions whose mass to charge ratio is higher than the parent ion (due to the loss of charge), but with the same mobility (unless ion evaporation occurs within the DMA itself, leading to mobilities intermediate for the parent and progeny ion mobilities[61]). In several instances, ion evaporation is coupled with neutral evaporation, leading to progeny ions which have lost a net amount $(AB)_m A^+$, where $m < N$. Again, without consideration of such reactions, line segments resulting from ion evaporation may be erroneously interpreted as evidence of multiple conformers for certain cluster ions. However, when both neutral and ion evaporation

are accounted for, only a single line segment, identifying clearly m/z and Z_p for cluster ions, remains. Therefore, with proper instrument calibration, CCS values are inferable for a large number of cluster ions of known m/z and z through use of eqn (1).

Comparison with gas molecule scattering calculations

Of primary interest in this work is the comparison of the CCS to the physical cross section (*i.e.* the orientationally averaged projected area, PA), both in measurements and in calculations, to examine the extent to which various impingement–reemission rules lead to CCSs in agreement with measured CCSs in N_2 and He. Therefore, the measured CCSs are normalized by projected areas, yielding for each ion the momentum scattering parameter $\Omega/\mathrm{PA} = \xi$. The projected area was determined for each ion by modeling it as a sphere, inferring a mass diameter d_i from the ion's density, ρ_{ion}, and then using the equation:[73]

$$\mathrm{PA} = \frac{\pi}{4}\left(d_i + d_g\right)^2 \quad (4)$$

where d_g is the gas molecule diameter, taken as 3.1 Å for N_2 and 2.4 Å for He. For each cluster, ρ_{ion} was inferred from the bulk density ρ_{bulk}, applying a correction factor for compressibility effects:[73,74]

$$\rho_{ion} = \frac{\rho_{bulk}}{1 - \dfrac{\Delta P}{K_0 + k_s \Delta P}}, \quad (5)$$

where K_0 is the bulk modulus and k_s is a pressure correction factor which are taken to be 3 and 5 GPa, respectively, for both RTILs.[62] ΔP is the Laplace pressure, which, when accounting for electrostatic forces (necessary when $z > 1$), is given by the equation:

$$\Delta P = \frac{4\gamma}{d_i} - \frac{z^2 e^2}{2\pi^2 \varepsilon_0 {d_i}^4}, \quad (6)$$

where γ is the surface tension (0.059 N m^{-1} at 295 K for EMIM-N(CN)$_2$ and 0.052 N m^{-1} at 295 K for EMIM-BF$_4$[75]) and ε_0 is the permittivity of free space (8.854×10^{-12} F m^{-1}). While considered in all calculations, the increase in density resulting from eqn (5) is at most 3% above the bulk density in the examined $z > 1$ ions. We elected not to compare $z = 1$ ions to calculations, as such clusters cannot be approximated by spheres, but note that for these cluster ions, eqn (5) predicts substantial increases in ion densities.

To calculate CCSs for simulated cluster ion structures, we used the program IMoS (freely available from the corresponding author, and described in detail previously[27–29]), which enables CCS determination from direct calculation of the rate of momentum transfer from gas molecules to candidate structures. Excess charges during the calculations were placed on the surface or in the center observing negligible differences. Similarly in analogous calculations, +1 and −1 charges were placed in every cation/anion finding minor differences with respect to just using excess charges. We specifically used 5 separate sets of impingement–reemission rules and ion–gas molecule potential interactions, denoted as follows:

TEHSS (trajectory-elastic hard sphere scattering). Gas molecule impingement and reemission is modeled as elastic and specular, with both the gas molecule and atoms within cluster ions modeled as hard spheres, but with the ion-induced dipole potential considered. For brevity, only the results using the polarizability of He (α = 0.2073 Å^3) with a gas radius of 1.2 Å (equivalent to that of He) are reported with this method.

TDHSS (trajectory-diffuse hard sphere scattering). Gas molecule impingement and reemission is modeled as inelastic and diffuse, with both the gas molecule and atoms within cluster ions modeled as hard spheres, but with the ion-induced dipole potential considered. The gas molecule is reemitted instantly after collision, with its speed sampled from a Maxwell–Boltzmann distribution with a most probable speed that is 8% less than expected at the surface temperature of the cluster ion, at a random angle from the cluster ion surface. As shown elsewhere,[28] this reemission choice will lead to ξ = 1.36 when applied to a spherical gas molecule and a smooth spherical ion, in the absence of potentials. For brevity, the results are shown only for the N_2 model, in which the gas molecule sphere of radius is 1.5 Å and the polarizability is α = 1.7 Å^3.

DHSS (diffuse hard sphere scattering). This method is identical to the TDHSS method, only with the ion-induced dipole potential neglected.

TMLJHe (trajectory method-Lennard-Jones-Helium). Lennard-Jones potentials (4-6-12) are employed in monitoring gas molecule trajectories, which leads to the implicit assumption of specular-elastic collisions. The Lennard-Jones pairs applied have been taken from the optimized values for He used by Campuzano *et al.*[7] Since the values for boron were unknown, σ = 3.043 Å and ε = 1.34 meV were used as initial approximations, but were not optimized.

TMLJN2 (trajectory method-Lennard-Jones-Nitrogen). This method is similar to the TMLJHe method, but with the optimized Lennard-Jones pairs for N_2 provided by Campuzano *et al.*[7] employed. Values of σ = 3.5 Å and ε = 2.60 meV were used for boron. Again, specular-elastic gas molecule scattering is implicitly assumed in this method.

For the TEHSS, TDHSS, and DHSS methods, atomic radii were taken from the values provided by Larriba & Hogan;[28] for boron and fluorine atoms the van der Waals radii were utilized. We remark, however, that for structures in the size range examined, the CCS is not a strong function of the atomic radii applied in calculations. All calculated CCSs are also normalized by PA, leading to ξ_{TEHSS}, ξ_{TDHSS}, ξ_{DHSS}, ξ_{TMLJHe}, and ξ_{TMLJN2}.

An additional comparison between measurement and theory is performed to examine the applicability of equations typically used to analyze mobility measurements in aerosol science and atmospheric chemistry. While in macromolecular and biomolecular analyses, most researchers opt to analyze mobility measurements *via* the Mason–Schamp equation (eqn (1)), and compare the resulting CCSs to predictions of a structural model[23,24,42] (as is performed here), in the study of aerosols, it is commonplace[76] to model measured ions (particles) as spheres and employ the experimentally derived Stokes–Millikan

(S–M) equation to compare the mobility Z_p with the particle diameter d_i:[49,77]

$$Z_p = \frac{ze}{3\pi\mu(d_i + d_g)}\left(1 + \frac{2\lambda}{d_i + d_g}\left(A_1 + A_2 e^{-\frac{A_3(d_i+d_g)}{\lambda}}\right)\right), \quad (7)$$

where μ is the gas dynamic viscosity, λ is the gas molecule mean free path, and A_1, A_2 and A_3 are dimensionless constants that have been inferred from multiple experiments (notably the work of Millikan,[47] which leads to A_1 = 1.257, A_2 = 0.4, and A_3 = 1.1) and agree well with direct simulation Monte Carlo modeling of non-continuum drag on particles.[43] This equation, which depends on the Knudsen number (Kn, the ratio of twice the surrounding gas mean free path to the sum of the particle and gas molecule diameters), can only be equivalent to eqn (1) in the so-called free molecular regime (Kn $\gg$ 1), as the Mason–Schamp equation only applies in this limit. Eqn (1) and (7) with Kn $\rightarrow \infty$ lead to the relationship:

$$\Omega_s = \frac{\pi}{4}\xi(d_p + d_g)^2 = \xi \mathrm{PA}. \quad (8)$$

With the values of A_1 and A_2 provided, ξ = 1.36 in eqn (8), which has been used almost without exception[5,16,18,50,54–56,59,61–63,78–81] with the Stokes–Millikan equation (for measurements in air and N_2). While Epstein[46] originally made arguments that ξ = 1.36 could arise if 91% of gas molecule–ion collisions were DHSS-like, with the remaining 9% EHSS-like, recently, we have shown that this argument only applies for smooth spherical ions with smooth spherical gas molecules,[30] and have further argued that it is not reasonable that gas molecules segregate themselves into two distinct populations, one colliding specularly and elastically and the second diffusely and inelastically, when both have the same speed distribution.[28] Therefore, the value ξ = 1.36 simply arises from an empirical observation. Nonetheless, we include it in comparison to measurements because of its prevalent use.

By directly transforming Fig. 3 contour plots, experimentally inferred values of ξ are plotted as a function of the square root of the cluster ion diameter in Fig. 4 (upper: EMIM-$N(CN)_2$ cluster ions; lower: EMIM-BF_4 cluster ions). Bands of specific charge states are still identifiable in plots, and are hence labelled. The calculation results are overlaid on Fig. 4 plots, and are additionally provided in Table 1. Immediately apparent is that for both RTILs, higher values of ξ are found for N_2 than in He, and that while ξ values in N_2 vary little with the mass diameter (oscillating between 1.35 and 1.44) or the charge state, there is a clear increase in ξ with the mass diameter in He (from 1.05 to 1.25 for the measured mass diameter range). Further evident is that for both RTILs, the calculated ξ values for TDHSS, DHSS, and TMLJN2 methods agree extremely well with N_2 gas experimental counterparts, and the predictions of the Kn $\rightarrow \infty$ limit of the Stokes–Millikan equation (ξ = 1.36) are in close agreement with measurements. Given that diffuse-inelastic gas-molecule reemission is employed in the TDHSS & DHSS methods, and noting that in prior work it has been shown that diffuse-inelastic scattering models do lead to relatively size invariant values of ξ 1.35–1.40,[27–29,43] the agreement

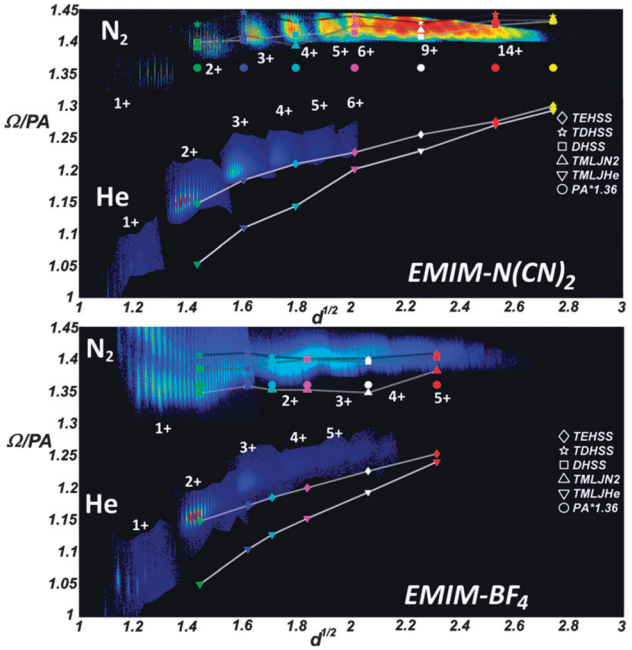

Fig. 4 Plot of the parameter $\xi = \Omega/\mathrm{PA}$ as a function of the square root of the mass diameter $d^{1/2}$ (where d is reported in nanometers) for EMIM-$N(CN)_2$ (top) and EMIM-BF_4 (bottom). Calculated CCSs are overlaid over the experimental results for selected potentials and impingement–reemission rules: TEHSS: specular-elastic (4-∞ potentials) – diamonds; TDHSS: diffuse-inelastic (4-∞ potentials) – stars; DHSS: diffuse-inelastic (hard sphere potentials) – squares; TMLJN2: N_2 Lennard-Jones potentials (4-6-12 potentials) – upright triangles; TMLJHe: He Lennard-Jones potentials (4-6-12 potentials) – downward triangles; PA*1.36: orientationally averaged projected area times 1.36 – circles.

in this instance is somewhat expected. The strong agreement between the results of TDHSS & DHSS methods shows that for the ions examined, the ion-induced dipole potential negligibly affects the CCS. More surprising is the mass diameter invariant value of ξ obtained by the TMLJN2 method, which utilizes optimized Lennard-Jones potentials. It appears that the use of such potentials leads to diffuse-like scattering, perhaps doing so by perturbing gas molecule trajectories such that they are reemitted from angles differing substantially from the hard-sphere specular angle due to the effect that the empirically-adapted strong potential wells of neighboring atoms has on the reemission of the gas molecules. Clearly, future work will be needed to resolve how this method reaches agreement with hard-sphere diffuse-inelastic methods over such a wide mass diameter range.

Equally interesting is the agreement found for TEHSS and TMLJHe methods with experimental results in He. This suggests that the drag enhancement effect brought about by multiple scattering (gas molecules impinging more than once) alone is sufficient to describe the increase in ξ above unity for organic ions in He experiments, while it alone cannot explain the value of ξ in diatomic N_2. Experimental and theoretical evidence for differences in the manner in which gas molecules impinge on and are reemitted from organic ions in these two gases can also be inferred from prior studies.[2,5,29,82] However, to the best of our knowledge, this is the only study which clearly

Table 1 Calculated collisional cross sections for all cases studied. Cluster ions are composed of N number of neutrals appearing on the first column for both RTILs, and with a charge state, z, in parenthesis. All CCSs are given in A^2, while ξ values are dimensionless. ξ results for calculations matching N_2 measurements are provided in the left ξ columns, while results matching He measurements are provided in the ξ columns on the right

	TMLJN2	DHSS	TDHSS	PA_{N2}	ξ_{TMLJN2}	ξ_{DHSS}	ξ_{TDHSS}	TMLJHe	TEHSS	PA_{He}	ξ_{TMLJHe}	ξ_{EHSS}
EMIM-N(CN)$_2$												
16(2)	615.3	618.9	631.6	442.3	1.39	1.40	1.43	440.0	479.5	418	1.05	1.15
32(3)	902.3	897.2	925	639.9	1.41	1.40	1.45	677.8	723.6	611.2	1.11	1.18
64(4)	1325	1342	1362	950.8	1.39	1.41	1.43	1035	1095	906.2	1.14	1.21
128(6)	2107	2090	2128	1478	1.43	1.41	1.44	1725	1763	1437	1.20	1.23
256(9)	3180	3157	3205	2243	1.42	1.41	1.43	2670	2725	2172	1.23	1.25
512(14)	4959	4934	5004	3461	1.43	1.43	1.45	4279	4298	3370	1.27	1.28
832(18)	7503	7578	7616	5295	1.42	1.43	1.44	6769	6793	5228	1.29	1.30
EMIM-BF_4												
18(1)	602.4	619.3	628.7	447.2	1.35	1.38	1.41	443.0	484.2	421.6	1.05	1.15
36(2)	938.9	957.6	974.6	691.4	1.36	1.38	1.41	731.4	776.4	661.9	1.10	1.17
50(2)	1137	1172	1180	840.6	1.35	1.39	1.40	908.8	955.3	805.9	1.13	1.19
78(2)	1438	1488	1490	1064	1.35	1.40	1.40	1184	1233	1027	1.15	1.20
156(3)	2226	2305	2314	1651	1.35	1.40	1.40	1909	1961	1599	1.19	1.23
312(5)	3453	3505	3521	2499	1.38	1.40	1.41	3025	3055	2438	1.24	1.25

displays these differences for ions with easily identifiable structures over a wide mass diameter range, and uses a variety of gas molecule scattering calculations for comparison with measurements.

While only subtly detected in measurements, we are also able to examine changes in ξ for ions of a specific charge state, z. In the case of EMIM-N(CN)$_2$ cluster ions in N_2, for each charge state there was a decrease in ξ with increasing mass diameter, which can be attributed to a reduced influence of the ion-induced dipole potential (which increases ξ when present[27,29,30,62,63]). However, for EMIM-BF_4 cluster ions in N_2, a minimum of ξ for each charge state is observed at a specific mass diameter, beyond which the ion-induced dipole potential is negligible and ξ starts to increase. This different observed behavior suggests that although in N_2 both RTIL cluster ions have similar values of ξ, the manner in which gas molecules are reemitted from them upon collision is not necessarily the same; there is no unique reemission angle distribution or velocity distribution which must apply to both ion types (or to any ion type). In the case of He, since the polarizability of the gas is an order of magnitude less than N_2, such an effect is negligible and only a steady rise in ξ is observed for a fixed charge state.

Finally, as a side note, the fact that both TMLJN2 and TMLJHe results in the case of EMIM-BF_4 are slightly less relative to the measurements than to EMIM-N(CN)$_2$ measurements suggests that the choice of the Lennard-Jones parameters for the boron atom was slightly smaller than optimal.

Measurement interpretation & implications

The measurements clearly show that gases used in this study have distinct mechanisms of reemission from organic ions, which directly influence the CCSs of such ions in these gases. He atoms appear to collide specularly and elastically, while diatomic N_2 appears to collide diffusely and inelastically. As a first approximation, there is a simple explanation for the differences observed in both gases. He is a light monoatomic atom (4 Da) with a high translational velocity (mean thermal speed of $\sim$1500 m s^{-1} near 300 K), while N_2 is a heavier diatomic gas (28 Da) with a more modest translational velocity ($\sim$500 m s^{-1} near 300 K). When a gas molecule impingement occurs upon a specific atom in an ion, which itself is vibrating, the momentum transferred (mass times velocity) by the N_2 gas molecule is much larger than that of the He atom. Given that most atoms in the cluster have less mass than that of the diatomic molecule, this invariably leads to a high probability for change in atomic trajectories (*i.e.* atomic internal energy) within ions. He atoms, conversely, are sufficiently light and fast, that their impingement does not disturb heavier atoms in an ion, leaving the reemission trajectories specular and elastic. This argument is additionally supported by recent measurements of the CCS of metal iodide salts in air; the closer the metal cation mass to N_2 and O_2, the larger the value of ξ observed.[29]

The differences in the Mason–Schamp and Stokes–Millikan equations can also be addressed by our results. The results suggest that the Stokes–Millikan equation remains valid in N_2 down to $\sim$1 nm in mass diameter and is equivalent to the Mason–Schamp equation in this instance. However, the Stokes–Millikan Kn $\rightarrow \infty$ limit does not appear to be applicable to ions measured in He spanning the entire mass diameter range examined here. As ξ increases with the mass diameter, it presumably reaches an asymptotic value in better agreement with Stokes–Millikan predictions.

Not addressed here, a correction factor would need to be introduced into the Stokes–Millikan equation for smaller or more highly charged species in diatomic gases, as in its conventional form, the influence of the ion-induced dipole potential is ignored (in eqn (4)). Furthermore, for lower molecular weight ions composed of cation–anion pairs, local electrostatic interactions between gas molecules and cations/anions may additionally influence CCSs.

Conclusions

The CCSs of RTIL cluster ions, generated by positive mode electrospray, have been measured in N_2 and He by DMA-MS and DT-MS respectively. The measured CCSs were normalized

by the calculated physical cross sections of ions (PA, projected area), yielding the parameter $\xi = \Omega/\mathrm{PA}$. ξ values were similarly estimated for candidate structures generated *via* molecular dynamics simulations, using gas molecule scattering calculations with a variety of impingement–reemission laws and gas molecule–ion potential interactions. Based on this study, we conclude:

(1) Diatomic N_2 collides non-specularly and inelastically with RTIL ions (with ions modeled as frozen structures), evidenced by the measured CCSs found to be in agreement with gas molecule scattering calculations utilizing hard sphere potentials, but wholly diffusive-inelastic, gas molecule impingement and reemission rules.

(2) Monoatomic He appears to collide almost perfectly specularly and elastically with the same ions, as measurements agree with elastic hard sphere scattering models.

(3) The difference in measured CCSs between the two gases cannot be attributed to gas molecule polarization, or to gas molecule size effects.

(4) Interestingly, trajectory methods for adjusted Lennard-Jones potentials can be used to mimic diffuse-inelastic gas molecule scattering calculations; specifically, trajectory method calculations using the potentials provided by Campuzano *et al.*[7] agree well with TDHSS and DHSS calculations.

(5) The difference in gas molecule impingement–reemission between the two gases can be rationalized as arising from the larger amount of momentum transferred per collision with N_2 as compared to He.

Acknowledgements

C. L. A. acknowledges support from a Ramon-Areces Fellowship. The authors additionally thank Prof. Juan Fernandez de la Mora (Yale University) for enlightening teaching and discussions on the nature of gas molecule–ion collisions.

References

1 T. L. Pukala, B. T. Ruotolo, M. Zhou, A. Politis, R. Stefanescu, J. A. Leary and C. V. Robinson, *Structure*, 2009, **17**, 1235–1243.
2 B. T. Ruotolo, J. L. P. Benesch, A. M. Sandercock, S. J. Hyung and C. V. Robinson, *Nat. Protoc.*, 2008, **3**, 1139–1152.
3 B. C. Bohrer, S. I. Merenbloom, S. L. Koeniger, A. E. Hilderbrand and D. E. Clemmer, *Annu. Rev. Anal. Chem.*, 2008, **1**, 293–327.
4 M. F. Bush, Z. Hall, K. Giles, J. Hoyes, C. V. Robinson and B. T. Ruotolo, *Anal. Chem.*, 2010, **82**, 9557–9565.
5 M. T. Bowers, *Int. J. Mass Spectrom.*, 2014, **370**, 75–95.
6 B. S. Kinnear, D. T. Kaleta, M. Kohtani, R. R. Hudgins and M. F. Jarrold, *J. Am. Chem. Soc.*, 2000, **122**, 9243–9256.
7 I. Campuzano, M. F. Bush, C. V. Robinson, C. Beaumont, K. Richardson, H. Kim and H. I. Kim, *Anal. Chem.*, 2012, **84**, 1026–1033.
8 Z. Hall, A. Politis, M. F. Bush, L. J. Smith and C. V. Robinson, *J. Am. Chem. Soc.*, 2012, **134**, 3429–3438.
9 K. Thalassinos, S. E. Slade, K. R. Jennings, J. H. Scrivens, K. Giles, J. Wildgoose, J. Hoyes, R. H. Bateman and M. T. Bowers, *Int. J. Mass Spectrom.*, 2004, **236**, 55–63.
10 M. Tam and H. H. Hill, *Anal. Chem.*, 2004, **76**, 2741–2747.
11 S. Trimpin and D. E. Clemmer, *Anal. Chem.*, 2008, **80**, 9073–9083.
12 S. Trimpin, M. Plasencia, D. Isailovic and D. E. Clemmer, *Anal. Chem.*, 2007, **79**, 7965–7974.
13 C. Larriba and J. Fernandez de la Mora, *J. Phys. Chem. B*, 2012, **116**, 593–598.
14 C. Larriba, J. Fernandez de la Mora and D. E. Clemmer, *J. Am. Soc. Mass Spectrom.*, 2014, **25**, 1332–1345.
15 J. Gidden, T. Wyttenbach, A. T. Jackson, J. H. Scrivens and M. T. Bowers, *J. Am. Chem. Soc.*, 2000, **122**, 4692–4699.
16 J. Jiang, J. Zhao, M. Chen, F. Eisele, J. H. Scheckman, B. J. Williams, C. Kuang and P. H. McMurry, *Aerosol Sci. Technol.*, 2011, **45**, ii–v.
17 M. Ehn, H. Junninen, S. Schobesberger, H. E. Manninen, A. Franchin, M. Sipila, T. Petaja, V. M. Kerminen, H. Tammet, A. Mirme, S. Mirme, U. Horrak, M. Kulmala and D. R. Worsnop, *Aerosol Sci. Technol.*, 2011, **45**, 522–532.
18 A. Kumar, S. Kang, C. Larriba-Andaluz, H. Ouyang, C. J. Hogan and R. M. Sankaran, *Nanotechnology*, 2014, **25**, 385601.
19 J. Fang, Y. Wang, M. Attoui, T. S. Chadha, J. R. Ray, W.-N. Wang, Y.-S. Jun and P. Biswas, *Anal. Chem.*, 2014, **86**, 7523–7529.
20 M. Westhoff, P. Litterst, L. Freitag, W. Urfer, S. Bader and J.-I. Baumbach, *Thorax*, 2009, **64**, 744–748.
21 S. Armenta, M. Alcala and M. Blanco, *Anal. Chim. Acta*, 2011, **703**, 114–123.
22 E. W. McDaniel and E. A. Mason, *The Mobility and Diffusion of Ions in Gases*, Wiley, New York, 1973.
23 M. F. Mesleh, J. M. Hunter, A. A. Shvartsburg, G. C. Schatz and M. F. Jarrold, *J. Phys. Chem.*, 1996, **100**, 16082–16086.
24 A. A. Shvartsburg and M. F. Jarrold, *Chem. Phys. Lett.*, 1996, **261**, 86–91.
25 A. A. Shvartsburg, B. Liu, M. F. Jarrold and K. M. Ho, *J. Chem. Phys.*, 2000, **112**, 4517–4526.
26 A. A. Shvartsburg, S. V. Mashkevich and K. W. M. Siu, *J. Phys. Chem. A*, 2000, **104**, 9448–9453.
27 C. Larriba and C. J. Hogan, *J. Comput. Phys.*, 2013, **251**, 344–363.
28 C. Larriba and C. J. Hogan, *J. Phys. Chem. A*, 2013, **117**, 3887–3901.
29 H. Ouyang, C. Larriba-Andaluz, D. R. Oberreit and C. J. Hogan, *J. Am. Soc. Mass Spectrom.*, 2013, **24**, 1833–1847.
30 H. Kim, H. I. Kim, P. V. Johnson, L. W. Beegle, J. L. Beauchamp, W. A. Goddard and I. Kanik, *Anal. Chem.*, 2008, **80**, 1928.
31 Y. Alexeev, D. G. Fedorov and A. A. Shvartsburg, *J. Phys. Chem. A*, 2014, **118**, 6763–6772.
32 A. A. Shvartsburg, B. Liu, K. W. M. Siu and K. M. Ho, *J. Phys. Chem. A*, 2000, **104**, 6152–6157.
33 B. T. Ruotolo, K. Giles, I. Campuzano, A. M. Sandercock, R. H. Bateman and C. V. Robinson, *Science*, 2005, **310**, 1658–1661.

34 C. J. Hogan, B. T. Ruotolo, C. V. Robinson and J. Fernandez de la Mora, *J. Phys. Chem. B*, 2011, **115**, 3614–4621.
35 J. Fernandez de la Mora and R. Borrajo, Z.-G. M., *J. Phys. Chem. B*, 2012, **116**, 9882–9898.
36 S. H. Chen, L. X. Chen and D. H. Russell, *J. Am. Chem. Soc.*, 2014, **136**, 9499–9508.
37 S. Vahidi, B. B. Stocks and L. Konermann, *Anal. Chem.*, 2013, **85**, 10471–10478.
38 A. R. Johnson, J. M. Dilger, M. S. Glover, D. E. Clemmer and E. E. Carlson, *Chem. Commun.*, 2014, **50**, 8849–8851.
39 H. L. Shi and D. E. Clemmer, *J. Phys. Chem. B*, 2014, **118**, 3498–3506.
40 F. Lanucara, S. W. Holman, C. J. Gray and C. E. Eyers, *Nat. Chem.*, 2014, **6**, 281–294.
41 E. van Duijn, A. Barendregt, S. Synowsky, C. Versluis and A. J. R. Heck, *J. Am. Chem. Soc.*, 2009, **131**, 1452–1459.
42 A. A. Shvartsburg, S. V. Mashkevich, E. S. Baker and R. D. Smith, *J. Phys. Chem. A*, 2007, **111**, 2002–2010.
43 C. Zhang, T. Thajudeen, C. Larriba, T. E. Schwartzentruber and C. J. Hogan, *Aerosol Sci. Technol.*, 2012, **46**, 1065–1078.
44 D. W. Mackowski, *J. Aerosol Sci.*, 2006, **37**, 242–259.
45 H. I. Kim, H. Kim, E. S. Pang, E. K. Ryu, L. W. Beegle, J. A. Loo, W. A. Goddard and I. Kanik, *Anal. Chem.*, 2009, **81**, 8289–8297.
46 P. S. Epstein, *Phys. Rev.*, 1924, **23**, 710–733.
47 R. A. Millikan, *Phys. Rev.*, 1923, **22**, 1–23.
48 J. H. Kim, G. W. Mulholland, S. R. Kukuck and D. Y. H. Pui, *J. Res. Natl. Inst. Stand. Technol.*, 2005, **110**, 31–54.
49 B. K. Ku and J. Fernandez de la Mora, *Aerosol Sci. Technol.*, 2009, **43**, 241–249.
50 C. Larriba, C. J. Hogan, M. Attoui, R. Borrajo, J. Fernandez-Garcia and J. Fernandez de la Mora, *Aerosol Sci. Technol.*, 2011, **45**, 453–467.
51 M. D. Allen and O. G. Raabe, *Aerosol Sci. Technol.*, 1985, **4**, 269–286.
52 H. Jung, K. Han, G. W. Mulholland, D. Y. H. Pui and J. H. Kim, *J. Aerosol Sci.*, 2013, **65**, 42–48.
53 P. Dugourd, R. R. Hudgins and M. F. Jarrold, *Chem. Phys. Lett.*, 1997, **267**, 186–192.
54 B. K. Ku, J. Fernandez de la Mora, D. A. Saucy and J. N. Alexander, *Anal. Chem.*, 2004, **76**, 814–822.
55 D. A. Saucy, S. Ude, I. W. Lenggoro and J. Fernandez de la Mora, *Anal. Chem.*, 2004, **76**, 1045–1053.
56 Z. G. Li and H. Wang, *Phys. Rev. E: Stat., Nonlinear, Soft Matter Phys.*, 2003, 68.
57 C. Larriba-Andaluz and C. J. Hogan, *J. Chem. Phys.*, 2014, **141**, 194107.
58 N. L. Zakharova, C. L. Crawford, B. C. Hauck, J. K. Quinton, W. F. Seims, H. H. Hill and A. E. Clark, *J. Am. Soc. Mass Spectrom.*, 2012, **23**, 792–805.
59 D. Hewitt, E. Marklund, D. J. Scott, C. V. Robinson and A. J. Borysik, *J. Phys. Chem. B*, 2014, **118**, 8489–8495.
60 C. J. Hogan and J. Fernandez de la Mora, *J. Am. Soc. Mass Spectrom.*, 2010, **21**, 1382–1386.
61 C. J. Hogan and J. Fernandez de la Mora, *Phys. Chem. Chem. Phys.*, 2009, **11**, 8079–8090.
62 J. Fernández-García and J. Fernández de la Mora, *J. Am. Soc. Mass Spectrom.*, 2013, **24**, 1872–1889.
63 J. Fernández-García and J. Fernández de la Mora, *Phys. Chem. Chem. Phys.*, 2014, **16**, 20500–20513.
64 J. Rus, D. Moro, J. A. Sillero, J. Royuela, A. Casado, F. Estevez-Molinero and J. Fernandez de la Mora, *Int. J. Mass Spectrom.*, 2010, **298**, 30–40.
65 J. Fernandez de la Mora, L. de Juan, T. Eichler and J. Rosell, *TrAC, Trends Anal. Chem.*, 1998, **17**, 328–339.
66 P. Dugourd, R. R. Hudgins, D. E. Clemmer and M. F. Jarrold, *Rev. Sci. Instrum.*, 1997, **68**, 1122–1129.
67 S. L. Koeniger, S. I. Merenbloom, S. J. Valentine, M. F. Jarrold, H. R. Udseth, R. D. Smith and D. E. Clemmer, *Anal. Chem.*, 2006, **78**, 4161–4174.
68 S. I. Merenbloom, S. L. Koeniger, S. J. Valentine, M. D. Plasencia and D. E. Clemmer, *Anal. Chem.*, 2006, **78**, 2802–2809.
69 C. S. Hoaglund, S. J. Valentine, C. R. Sporleder, J. P. Reilly and D. E. Clemmer, *Anal. Chem.*, 1998, **70**, 2236–2242.
70 A. E. Counterman, S. J. Valentine, C. A. Srebalus, S. C. Henderson, C. S. Hoaglund and D. E. Clemmer, *J. Am. Soc. Mass Spectrom.*, 1998, **9**, 743–759.
71 N. L. Allinger, *J. Am. Chem. Soc.*, 1977, **99**, 8127–8134.
72 Ionic Liquid Database. Available from: http://ilthermo.boulder.nist.gov/.
73 P. G. Tait, *Scientific papers*, The Cambridge University Press, Cambridge, 1900, vol. II.
74 A. T. J. Hayward, *Br. J. Appl. Phys.*, 1967, **18**, 965–977.
75 C. Larriba, Y. Yoshida and J. Fernández de la Mora, *J. Phys. Chem. B*, 2008, **112**, 12401–12407.
76 H. Tammet, *J. Aerosol Sci.*, 1995, **26**, 459–475.
77 C. N. Davies, *Proc. Phys. Soc.*, 1945, **57**, 259–270.
78 D. R. Oberreit, P. H. McMurry and C. J. Hogan, *Phys. Chem. Chem. Phys.*, 2014, **16**, 6968–6979.
79 A. Maiser, V. Premnath, A. Ghosh, T. A. Nguyen, M. Attoui and C. J. Hogan, *Phys. Chem. Chem. Phys.*, 2011, **13**, 21630–21641.
80 A. J. Borysik and C. V. Robinson, *Phys. Chem. Chem. Phys.*, 2012, **14**, 14439–14449.
81 Z. Li and H. Wang, *Phys. Rev. E: Stat., Nonlinear, Soft Matter Phys.*, 2003, **68**, 061206.
82 F. A. Fernandez-Lima, C. Becker, K. Gillig, W. K. Russell, M. A. C. Nascimento and D. H. Russell, *J. Phys. Chem. A*, 2008, **112**, 11061–11066.